

Dependency of Mesoscale Organization on Grid Anisotropy in Large-Eddy Simulations of Convective Boundary Layers at Gray Zone Resolutions

de Roode, S.R.; Siebesma, A.P.; Jansson, F.R.; Janssens, Martin

DOI

[10.1029/2022MS003095](https://doi.org/10.1029/2022MS003095)

Publication date

2022

Document Version

Final published version

Published in

Journal of Advances in Modeling Earth Systems

Citation (APA)

de Roode, S. R., Siebesma, A. P., Jansson, F. R., & Janssens, M. (2022). Dependency of Mesoscale Organization on Grid Anisotropy in Large-Eddy Simulations of Convective Boundary Layers at Gray Zone Resolutions. *Journal of Advances in Modeling Earth Systems*, 14(11), Article e2022MS003095. <https://doi.org/10.1029/2022MS003095>

Important note

To cite this publication, please use the final published version (if applicable).
Please check the document version above.

Copyright

Other than for strictly personal use, it is not permitted to download, forward or distribute the text or part of it, without the consent of the author(s) and/or copyright holder(s), unless the work is under an open content license such as Creative Commons.

Takedown policy

Please contact us and provide details if you believe this document breaches copyrights.
We will remove access to the work immediately and investigate your claim.

RESEARCH ARTICLE

10.1029/2022MS003095

Key Points:

- A grid anisotropy factor is introduced to efficiently switch from an isotropic to an anisotropic eddy diffusion approach for large-eddy simulation models
- The organization of clear boundary-layer convection depends on the horizontal grid spacings, most notably for the anisotropic eddy diffusion approach
- Reduced variances at the smallest length scales may be compensated by opposite increases at larger length scales

Correspondence to:

S. R. de Roode,
s.r.derode@tudelft.nl

Citation:

de Roode, S. R., Siebesma, A. P., Jansson, F., & Janssens, M. (2022). Dependency of mesoscale organization on grid anisotropy in large-eddy simulations of convective boundary layers at Gray Zone resolutions. *Journal of Advances in Modeling Earth Systems*, 14, e2022MS003095. <https://doi.org/10.1029/2022MS003095>

Received 18 MAR 2022




Accepted 9 AUG 2022

Author Contributions:

Investigation: Martin Janssens
Methodology: A. Pier Siebesma, Fredrik Jansson, Martin Janssens
Writing – review & editing: Fredrik Jansson, Martin Janssens

© 2022 The Authors. Journal of Advances in Modeling Earth Systems published by Wiley Periodicals LLC on behalf of American Geophysical Union. This is an open access article under the terms of the [Creative Commons Attribution-NonCommercial-NoDerivs License](#), which permits use and distribution in any medium, provided the original work is properly cited, the use is non-commercial and no modifications or adaptations are made.

Dependency of Mesoscale Organization on Grid Anisotropy in Large-Eddy Simulations of Convective Boundary Layers at Gray Zone Resolutions

Stephan R. de Roode¹ , A. Pier Siebesma^{1,2}, Fredrik Jansson¹ , and Martin Janssens^{1,3} 

¹Delft University of Technology, Delft, The Netherlands, ²KNMI, De Bilt, The Netherlands, ³Wageningen University, Wageningen, The Netherlands

Abstract A new generation of operational atmospheric models operating at horizontal resolutions in the range 200 m ~ 2 km is becoming increasingly popular for operational use in numerical weather prediction and climate applications. Such grid spacings are becoming sufficiently fine to resolve a fraction of the turbulent transports. Here we analyze Large-eddy simulation results of a convective boundary layer obtained by coarsening horizontal grid spacings up to 800 m. The aim is to explore the dependency of the mean state and turbulent fluxes on the grid resolution. Both isotropic and anisotropic eddy diffusion approaches are evaluated, where in the latter case the horizontal and vertical eddy diffusivities differ in accord with their horizontal and vertical grid spacings. For coarsening horizontal grid sizes entrainment at the top of the boundary layer tends to get slightly enhanced for isotropic diffusion, whereas for the anisotropic diffusion approach the vertically well-mixed boundary-layer structure becomes severely degraded. An analysis of the energy spectrum shows that anisotropic diffusion causes relatively more dissipation of variance at smaller length scales. This leads, in turn, to a shift of spectral energy toward larger length scales that also becomes apparent from a rather different kind of spatial organization of convection. The present study therefore suggests that details with regards to the representation of processes at small scales might impact the organization at length scales much larger than the smallest scales that can be resolved by the model.

Plain Language Summary A new generation of operational atmospheric models operating at horizontal resolutions in the range 200 m ~ 2 km is becoming increasingly popular for operational use in numerical weather prediction and climate applications. Owing to ever increasing computational power their grid spacings are nowadays becoming sufficiently fine to allow for resolving a fraction of the turbulent transports. However, these types of models are operated with grid spacings that are much larger in the horizontal directions than in the vertical direction. In the present study we explore the extent to which the spatial organization of turbulence structures is affected by the size of the horizontal grid spacing. This question is addressed by means of large-eddy simulation, which is an established modeling technique that has been designed specifically to resolve the dominant turbulent eddies at a high spatial resolution. It is found that differences in the way how turbulence at scales smaller than the grid spacing is calculated can have an effect on the organization of turbulent structures at much larger spatial scales.

1. Introduction

Numerical simulations of atmospheric turbulence can be performed with models whose spatial resolutions are sufficiently fine to resolve the dominant turbulent eddies. Large-eddy simulation (LES) is an important and widely used technique in this respect. LES is nowadays used to successfully reproduce a wide range of atmospheric flow regimes including the transition from a stable to a convective boundary layer van Hooft et al. (2019), shallow and deep convective clouds (Wing et al., 2020), as well as flows in urban areas (Grylls et al., 2020; Hellsten et al., 2020). The skill with which they can faithfully capture observations has been addressed in various model intercomparison studies including the clear convective boundary layer (Nieuwstadt et al., 1993), the stable boundary layer (Beare et al., 2006), precipitating shallow cumulus (Van Zanten et al., 2011), and the transition of stratocumulus to shallow cumulus (Van der Dussen et al., 2013). As a result LES is becoming an increasingly more powerful tool for operational use in weather and climate applications and are used as high resolution limited area models embedded in larger scale atmospheric models (Draxl et al., 2021; Heinze et al., 2017; Ovchinnikov et al., 2022; Schalkwijk et al., 2015).

The supercomputing facilities nowadays allow operating numerical global weather forecast models at sub-kilometer scales, which enables them to resolve some fraction of the turbulent eddies. In the latter case parameterizations that were developed for turbulent transport in large-scale models need to be adapted, basically because the implicit assumption that the turbulent transports are entirely due to the unresolved, subgrid fluctuations becomes violated (Honnert et al., 2020). This question has motivated Boutle et al. (2014) to design a new scale-aware parameterization that is in part inspired by LES subgrid turbulent kinetic energy (TKE) models.

An aspect of modeling convection in this “Gray Zone” that has received little attention is that LES models often apply anisotropic grids. In practice this implies that the applied grid spacing in the horizontal direction is typically much coarser than in the vertical direction. Such a choice is motivated by the need, on the one hand, to resolve sharp vertical gradients such as present near the ground surface and thermal inversion layers, and, on the other hand, to capture a sufficient number of large eddies in the LES domain. For example, LES models that participated in the model intercomparison study of a convective boundary layer by Nieuwstadt et al. (1993) applied horizontal and vertical domain sizes $L_{\text{hor}} = 6.4$ km and $L_{\text{ver}} = 2.4$ km, respectively, and horizontal and vertical grid spacings $\Delta x_{\text{hor}} = 160$ m and Δz as fine as 20 m near the surface, respectively.

The contribution of the unresolved eddies to the turbulent transports as well as their dissipation by molecular viscosity can be parameterized in LES models with use of a subgrid TKE model. The subgrid turbulent fluxes are typically taken to be proportional to an eddy diffusivity factor, which depends on the intensity of the unresolved velocity fluctuations as quantified by the subgrid TKE, and a turbulent length scale that depends on the horizontal and vertical grid spacings (Deardorff, 1980). Even though the grid may be anisotropic, LES models may apply an isotropic diffusion approach. The latter means that they apply an equal value for the eddy diffusion in all the three directions.

The present study is in part inspired by Van Zanten (2000) who noted a sensitivity of LES results on the size of the horizontal grid spacing (her Chapter 5). She performed simulations of a clear convective boundary layer with rather modest variations in the horizontal grid spacings, in the range from 12.5 up to 50 m. Van Zanten performed her simulations with use of the subgrid model of Deardorff (1980), and found larger entrainment fluxes at the top of the boundary layer with coarsening horizontal grid spacings. The deviating results with respect to the run with the highest spatial resolution could be attributed to enhanced subgrid turbulent fluxes, in accord with the design of the subgrid model, that were however not accompanied by an opposing decrease in the resolved turbulent fluxes. In other words, the applied subgrid model is not capable to consistently partition the subgrid and resolved contributions to the total fluxes for varying horizontal grid spacings. Another problem related to the grid configuration has been discussed by De Roode et al. (2017). They explained from a comparison of Monin-Obukhov similarity theory with analytical subgrid TKE solutions, that were obtained from an assumed balance between the buoyancy flux, shear production and dissipation of subgrid TKE, that the application of anisotropic grids with isotropic subgrid diffusion leads to an enhancement of turbulent diffusion that actually can be excessively strong to eliminate any resolved fluctuations in the temperature and velocity fields in the stable boundary layer.

Motivated by the findings of Van Zanten (2000) and De Roode et al. (2017) we have studied the behavior of the isotropic and anisotropic diffusion approaches for anisotropic grids with the Dutch Atmospheric Large Eddy Simulation (DALES) model (Arabas et al., 2021; Heus et al., 2010). The current DALES code applies the isotropic diffusion approach following Deardorff (1980) and is identical to the scheme studied earlier by Van Zanten (2000). However, for the present study DALES has been elaborated with an anisotropic diffusion approach following the System for Atmospheric Modeling (SAM) LES model (Stevens, Vali, et al., 2005) and similar to the Weather Research and Forecasting (WRF) LES model (Simon & Chow, 2021).

In this study we investigate the behavior of the isotropic and anisotropic diffusion approaches for coarsening horizontal grid sizes, toward values that are currently feasible for NWP models. Because subgrid diffusion tends to smooth out resolved fluctuations at the smallest length scales, we are particularly interested in the question as to how this affects the energy spectra and the organization of turbulence structures. To this end, we simulated a clear convective boundary layer with DALES with horizontal grid spacings ranging from isotropic to extremely anisotropic, $\Delta x_{\text{hor}} = 12.5$ and 800 m, respectively. Section 2 will introduce a grid anisotropy factor that can be used to efficiently switch from an isotropic to an anisotropic diffusion approach, with the latter similar to what is applied by the SAM LES model. The case set up is briefly explained in Section 3, next the results are presented and discussed in Section 4, and Section 5 gives a summary and conclusions.

2. A Comparison of the Isotropic and Anisotropic Subgrid Diffusion Approaches

Here we will consider an anisotropic grid which has the same size Δx_{hor} in both horizontal directions, $\Delta x = \Delta y = \Delta x_{\text{hor}}$, but whose vertical mesh size is smaller than the horizontal ones, a configuration that is typical for LES applications of atmospheric systems, $\Delta x_{\text{hor}} \geq \Delta z$. As opposed to the isotropic diffusion approach, an anisotropic subgrid scheme applies an eddy viscosity, and similarly an eddy diffusivity, that depends on the direction to which it is applied, with its magnitude being dependent on the grid spacing in the respective direction. Here we will compare the isotropic subgrid diffusion scheme as proposed by Deardorff (1980) with an anisotropic diffusion approach that is, as an example, applied in the SAM LES model (Khairoutdinov & Randall, 2005; Stevens, Moeng, et al., 2005).

2.1. LES Budget Equations

Models that are applied to simulating atmospheric motions apply the conservation equations of momentum, heat, and the total water specific humidity, which can generally be expressed as

$$\frac{d\varphi}{dt} = \frac{\partial \varphi}{\partial t} + u_j \frac{\partial \varphi}{\partial x_j} = S_\varphi, \quad (1)$$

with t the time, φ an arbitrary prognostic variable, the velocity vector components $(u_1, u_2, u_3) = (u, v, w)$ in the (x, y, z) direction, respectively, with z the vertical direction, and S_φ a source term. LES models apply filtered equations in which the prognostic variables are decomposed in so-called resolved ($\tilde{\varphi}$) and subgrid fluctuations (φ''), that is, $\varphi = \tilde{\varphi} + \varphi''$ (Leonard, 1974). The subgrid fluctuations are associated with unresolved structures that have length scales that are close to the applied grid spacing. Application of the filter to the conservation Equation 1, and assuming that filtering and differentiation commute, gives

$$\frac{\partial \tilde{\varphi}}{\partial t} = -\frac{1}{\rho_0} \frac{\partial \rho_0 \tilde{u}_j \tilde{\varphi}}{\partial x_j} - \frac{1}{\rho_0} \frac{\partial \rho_0 \widetilde{u_j'' \varphi''}}{\partial x_j} + \tilde{S}_\varphi, \quad (2)$$

where the conservation equation for mass is applied to express the advection term in flux form. Here $\rho_0(z)$ is the reference density profile. The filter operation gives rise to the second term on the right-hand side, which represents the effect of subgrid-scale flux transport. Following the downgradient diffusion approach it is computed for scalars as

$$\widetilde{u_j'' \varphi''} = -K_h \frac{\partial \tilde{\varphi}}{\partial x_j}, \quad (3)$$

with K_h the eddy diffusivity, whereas the subgrid momentum fluxes depend on the eddy viscosity K_m according to,

$$\widetilde{u_i'' u_j''} = -K_m \left(\frac{\partial \tilde{u}_i}{\partial x_j} + \frac{\partial \tilde{u}_j}{\partial x_i} \right), \quad (4)$$

with

$$K_{m,h} = c_{m,h} \sqrt{e} \ell. \quad (5)$$

Here ℓ is a length scale and $c_{m,h}$ is a proportionality constant that is applied to a scalar (c_h) or momentum (c_m). They are related through the turbulent Prandtl number according to $\text{Pr} = c_m/c_h$ that is set to a value of 1/3 in DALES. Because the eddy viscosity and diffusivity differ only by a fixed factor, statements regarding the eddy diffusivity made in the present paper are generally also applicable to the eddy viscosity and will therefore not be repeated for the latter. The filtered subgrid TKE (e) can, in turn, be computed from its budget equation (Deardorff, 1980),

$$\frac{\partial e}{\partial t} + \frac{1}{\rho_0} \frac{\partial \rho_0 \tilde{u}_j e}{\partial x_j} = \frac{g}{\theta_0} \widetilde{w'' \theta_v''} - \widetilde{u_i'' u_j''} \frac{\partial \tilde{u}_i}{\partial x_j} - \frac{1}{\rho_0} \frac{\partial}{\partial x_j} \left(\rho_0 \widetilde{u_j'' e} + \widetilde{u_j'' p''} \right) - \epsilon, \quad (6)$$

with θ_v the virtual potential temperature, θ_0 the reference profile of the virtual potential temperature, p the pressure and ϵ the viscous dissipation term.

The subgrid buoyancy and momentum fluxes are computed from Equations 3 and 4, respectively. The total subgrid turbulent transport term can be computed following a downgradient diffusion approach,

$$\widetilde{u_j''e} + \frac{\widetilde{u_j''p''}}{\rho_0} = -2K_m \frac{\partial e}{\partial x_j}. \quad (7)$$

In DALES for practical, numerical reasons the budget equation for e is divided by the square root of the subgrid TKE. The subgrid diffusion of subgrid TKE as presented in the equation above is actually applied to \sqrt{e} rather than e itself (Cuijpers and Duynkerke 1993, see their Equation 12). The viscous dissipation term ϵ is calculated as

$$\epsilon = c_\epsilon \frac{e^{3/2}}{\lambda_\epsilon}, \quad (8)$$

with c_ϵ a proportionality constant and λ_ϵ a length scale. The values of the subgrid constants as applied in DALES are summarized in De Roode et al. (2017).

2.1.1. Isotropic Diffusion Approach

The isotropic diffusivity approach uses $\ell = \lambda_\epsilon = l_\Delta$ (Deardorff, 1980), with

$$l_\Delta \equiv (\Delta x \Delta y \Delta z)^{1/3}, \quad (9)$$

to give

$$K_{m,h} = c_{m,h} l_\Delta \sqrt{e}. \quad (10)$$

It follows from the definition Equation 9 that an anisotropic grid spacing has an implicit impact on the subgrid diffusion. For example, a stretching of the horizontal grid spacing causes l_Δ to increase, and this will consequently lead to an increase of $K_{m,h}$. This implies that the eddy diffusivity, even if it is applied isotropically, will also be enhanced for the vertical subgrid eddy transport even if the vertical grid spacing is not modified. The physical reason for this dependency is that the subgrid-scale eddy sizes that are captured in a grid box are enlarged with increasing horizontal grid spacing, and consequently their enhanced capacity to transport properties is taken into account in this way.

2.1.2. Anisotropic Diffusion Approach

Here we adopt the anisotropic diffusion approach used in the SAM LES model as described in the Appendix A of Stevens, Moeng, et al. (2005). The eddy diffusivity that is applied in the vertical direction uses Δz as a length scale, which gives

$$K_{m,h,vert} = c_{m,h} \Delta z \sqrt{e}. \quad (11)$$

The horizontal eddy diffusivity $K_{m,h,hor}$ is computed by multiplying $K_{m,h,vert}$ by a square of the ratio of horizontal to vertical grid spacings,

$$K_{m,h,hor} = K_{m,h,vert} \left(\frac{\Delta x_{hor}}{\Delta z} \right)^2. \quad (12)$$

Following the SAM LES model formulation, the length scale that is used to compute the subgrid TKE is based on the size of the minimum grid spacing in all the three directions. Because it is common practice in atmospheric LES applications to apply a mesh with $\Delta z \leq \Delta x_{hor}$, such a configuration will be assumed in the remainder of the text. This implies that the subgrid TKE is computed according to Equation 6 with $\ell = \lambda_\epsilon = \Delta z$, and with an isotropic eddy diffusivity that depends on this length scale as $K_{m,h} = c_{m,h} \Delta z \sqrt{e}$.

2.2. Analytical Solutions for the Eddy Diffusivity

In the following we will compare the analytical solutions for the isotropic and anisotropic eddy diffusivities under the assumption of a balance between subgrid TKE production by shear and buoyancy, and a loss by viscous dissipation. These three terms comprise the Smagorinsky subgrid model with stability correction (Mason, 1989), which assumes a steady state for e and ignores the mean advection and total turbulent transport of subgrid TKE. In the analytical solutions we will apply the following definitions for the resolved flow rate of strain tensor S and the Brunt-Väisälä frequency N , respectively,

$$S^2 \equiv \frac{1}{2} \left(\frac{\partial u_j}{\partial x_i} + \frac{\partial u_i}{\partial x_j} \right)^2 \quad (13)$$

$$N \equiv \left(\frac{g}{\theta_0} \frac{\partial \theta_v}{\partial z} \right)^{1/2}. \quad (14)$$

The Smagorinsky subgrid TKE equation with buoyancy production can then be expressed as

$$-K_h N^2 + K_m S^2 - c_\epsilon \frac{e^{3/2}}{\lambda_\epsilon} = 0. \quad (15)$$

For an easy comparison of the analytical solutions we introduce a factor r that gives a measure of the grid anisotropy,

$$r \equiv \frac{\Delta x_{\text{hor}}}{\Delta z}. \quad (16)$$

2.2.1. Isotropic Diffusion

For the Smagorinsky model including buoyancy production, and with aid of the anisotropy factor r , analytical solutions for the subgrid TKE and eddy diffusivity can be expressed as, respectively,

$$e = C_{\text{stab}} r^{4/3} \Delta z^2 S^2, \quad (17)$$

$$K_{m,h} = c_{m,h} C_{\text{stab}}^{1/2} r^{4/3} \Delta z^2 S. \quad (18)$$

with C_{stab} a factor that involves the subgrid model constants and which depends on the local stability as measured by N^2/S^2 ,

$$C_{\text{stab}} = \frac{c_m}{c_\epsilon} \left(1 - \frac{c_h}{c_m} \frac{N^2}{S^2} \right). \quad (19)$$

It is clear that an increase in the grid anisotropy factor r will yield a larger eddy diffusivity.

2.2.2. Anisotropic Diffusion

The analytical solution for the subgrid TKE reads

$$e = C_{\text{stab}} \Delta z^2 S^2, \quad (20)$$

which can be used to express the vertical and horizontal diffusivities as, respectively,

$$K_{m,h,\text{vert}} = c_{m,h} C_{\text{stab}}^{1/2} \Delta z^2 S, \quad (21)$$

$$K_{m,h,\text{hor}} = c_{m,h} C_{\text{stab}}^{1/2} r^2 \Delta z^2 S. \quad (22)$$

A comparison of the solutions Equations 18 and 21 shows that for $r > 1$, or equivalently $\Delta x_{\text{hor}} > \Delta z$, the anisotropic vertical diffusivity is smaller than the isotropic value. By contrast, a stretching of the horizontal grid spacing will yield a larger diffusivity to be applied in the horizontal direction Equation 22 as compared to the isotropic diffusivity Equation 18.

Table 1
Summary of the Horizontal Grid Spacings Δx_{hor} Applied in the Large-Eddy Simulations

Isotropic diffusion	Anisotropic diffusion	Δx_{hor} (m)	Anisotropy factor $r = \Delta x_{\text{hor}}/\Delta z$
H289	—	12.5	1
H410	H420	25	2
H411	H421	50	4
H412	H422	100	8
H413	H423	200	16
H414	H424	400	32
H415	H425	800	64

Note. For all the simulations the vertical grid spacing $\Delta z = 12.5$ m, and the horizontal and vertical domain sizes are 12.8^2 km^2 and 1,593.75 m, respectively. The isotropic diffusion approach refers to the application of Equation 10, whereas the anisotropic diffusion approach allows for different values in the vertical and horizontal directions according to Equations 11 and 12, respectively.

2.2.3. Practical Implementation

The original DALES code has been elaborated with the anisotropic diffusion approach with just a few minor modifications at two parts. The first change involves the choice of the length scale to be used in the subgrid TKE equation. We use either $\ell = \lambda_e = l_\Delta$ as a length scale to compute the isotropic diffusivity, or otherwise $\ell = \lambda_e = \Delta z$ to obtain the subgrid TKE needed for determining the horizontal and vertical diffusivities. The second change involves a multiplication of the horizontal subgrid fluxes that are present in the budget equations for all the prognostic variables, except for the subgrid TKE, with the grid anisotropy factor r^2 . This gives the desired enhancement of the horizontal diffusivity for the anisotropic diffusion approach.

3. Set up of the Experiments

To compare the performance of the isotropic and anisotropic diffusion approaches we have performed runs of a clear convective boundary layer. Similar to the Gray Zone LES numerical experiments that were carried out by Efsthathiou et al. (2016) and Doubrawa and Muñoz-Esparza (2020), sensitivity experiments were performed in which the horizontal grid spacing was systematically coarsened. The setup of the simulations is presented below.

3.1. Initial and Boundary Conditions

The CBL is forced by constant homogeneous surface fluxes $\overline{w'\theta'}_{\text{sfc}} = 0.1 \text{ mKs}^{-1}$ and $\overline{w'q'}_{\text{sfc}} = 2 \times 10^{-5} (\text{kg kg}^{-1}) \text{ ms}^{-1}$. The initial potential temperature and water vapor specific humidity are constant with values of 293 K and 8 g kg⁻¹, respectively, up to the top of the boundary layer that is located at a height of 493.75 m. The inversion layer with initial thickness of 12.5 m has initial jump values $\Delta\theta = 5.04 \text{ K}$ and $\Delta q_v = -4 \text{ g kg}^{-1}$. The free tropospheric humidity is set to a constant value of 4 g kg⁻¹, whereas the vertical gradient of θ is set to 6 K km⁻¹ above the inversion layer. The geostrophic wind is constant with height (U_g, V_g) = (1, 0) m s⁻¹, and the initial horizontal wind is set equal to the geostrophic wind. To spin up turbulence random perturbations with maximum values of 0.1 K and $10^{-3} \text{ g kg}^{-1}$ were added to the initial fields of θ and q_v , respectively. A constant value of $1 \text{ m}^2 \text{ s}^{-2}$ for the initial subgrid TKE in the boundary layer is prescribed.

3.2. Grid Configurations

A reference simulation was performed with $\Delta x_{\text{hor}} = \Delta z = 12.5$ m. Table 1 gives a summary of the sensitivity experiments. The grid anisotropy factor r was gradually increased by systematically doubling the horizontal grid spacings from 25 up to 800 m while maintaining the same domain size (12.8 km in both horizontal directions) and vertical grid spacing ($\Delta z = 12.5$ m). By restricting ourselves to a fixed value for Δz we avoid additional model sensitivities to changes in the vertical resolution, such as, for example, the entrainment rate (Sullivan & Patton, 2011). We note that the extremely large grid anisotropy values were merely applied to explore different

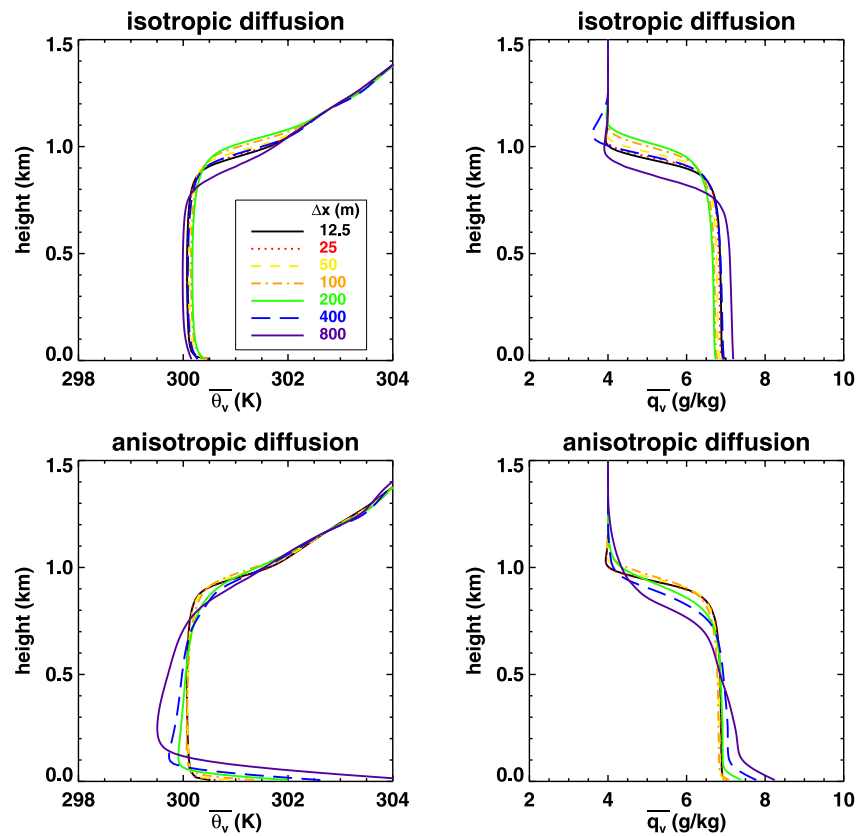


Figure 1. Vertical profiles of the horizontal slab mean values of the virtual potential temperature $\bar{\theta}_v$ and water vapor specific humidity \bar{q}_v during the 8th hr of the simulation. The two upper plots show simulation results for isotropic diffusion with l_Δ as a length scale, and the lower two plots were obtained for anisotropic diffusion. The horizontal grid spacings are according to the legend.

behaviors in the isotropic and anisotropic diffusivities. Because of the fixed horizontal domain size the simulations with a stretched horizontal grid were performed with a reduced number of grid points in the horizontal directions, down to only 16^2 for the coarsest cases. As a check to verify whether this choice did not impact the results, the simulations were also repeated with a minimum number of 128 grid points in both horizontal directions. We found that the latter results were qualitatively similar in terms of the mean state, turbulent flux profiles and visualizations of instantaneous fields. All simulations were performed with a variance-preserving second-order advection scheme.

4. Results

Here we will compare the results of the runs in terms of the representation of the mean state, the vertical profiles of the turbulent fluxes of heat and moisture, and turbulence. We will discuss how the entrainment rate at the top of the boundary layer is affected by the particular choice of the eddy diffusion approach. The second part of the analysis will focus on the organization of turbulent structures by a visual inspection of some fields in the middle of the boundary layer in addition to a quantification of the spectral energy densities.

4.1. Mean State and Turbulence Structure

Figure 1 compares the mean state results of the virtual potential temperature $\bar{\theta}_v$ and the water vapor specific humidity \bar{q}_v as obtained with different horizontal grid spacings. For $\Delta x_{\text{hor}} \leq 100$ m the mean vertical profiles for $\bar{\theta}_v$ and \bar{q}_v in the boundary layer remain very close to the Reference run results.

The results show that the kind of diffusion approach can affect the vertical mean state of the boundary layer. In general convective boundary layers are characterized by vertically well mixed states for quantities like θ_v and q_v , and such properties are well captured in the simulations that applied the isotropic diffusion approach. By contrast, for the anisotropic diffusion approach the vertical mean profiles for θ_v and q_v start to deviate significantly from a vertical well mixed state for coarsening horizontal grid spacing. Most notably a stable stratification, as quantified by a positive slope in θ_v , has developed rather close to the surface in the simulations with the coarsest values for Δx_{hor} . This finding strongly resembles the results that were obtained by Simon and Chow (2021) who used the WRF LES model with the anisotropic diffusion approach for $\Delta x_{\text{hor}} = 1.2$ km, see their Figures 3e and 3f. Later on in the text we will discuss the cause of the stable stratification as well as its impact on the subgrid TKE and the resulting eddy diffusivities.

The isotropic diffusion approach tends to produce slightly deeper, drier and warmer boundary layers for anisotropic grid spacings up to $\Delta x_{\text{hor}} \leq 200$ m. These deviations from the Reference case results can be explained from the relation between the growth rate of boundary layer depth (h) and the entrainment velocity (w_e),

$$\frac{dh}{dt} = w_e. \quad (23)$$

Entrainment is a process in which turbulent eddies penetrate into the inversion layer, and subsequently engulf and mix some of the relatively warm and dry inversion air downwards into the boundary layer (Sullivan et al., 1998). Larger entrainment rates therefore explain why deeper boundary layers tend to be relatively warmer and drier. For $r \leq 16$ enhanced entrainment rates might be explained from the fact that, according to Equation 18, the isotropic eddy diffusivity will tend to increase for increasing grid anisotropy factor r .

The application of extremely anisotropic grids, $\Delta x_{\text{hor}} \geq 400$ m, causes a slower growth of the boundary layer depth both for the isotropic and anisotropic diffusion approach. Because entrainment is driven by strong updrafts that penetrate the inversion layer, the slower growth rate of the boundary layer depth could possibly be explained by the resolved vertical velocity variances, which become notably smaller for coarsening horizontal grid spacings (see Figures 2 and 3).

Figures 2 and 3 show vertical profiles of turbulent fluxes as obtained with the isotropic and anisotropic diffusion approaches, respectively. In addition to the total (“tot”) fluxes of the potential temperature and water vapor specific humidity their subgrid (“sub”) and resolved (“res”) contributions are also presented,

$$\overline{w'\varphi'}_{\text{tot}} = \overline{w'\varphi'}_{\text{sub}} + \overline{w'\varphi'}_{\text{res}}. \quad (24)$$

There is a rather strong difference in the subgrid contributions to the total vertical turbulent fluxes of θ_v and q_v in the sense that for the anisotropic diffusion approach the subgrid flux contributions are mainly dominant in the lower part of the boundary layer. For the isotropic diffusion approach the subgrid fluxes become gradually more important and tend to extend toward the middle of the boundary layer for coarsening horizontal grid spacings.

Like the vertical fluxes the total TKE also includes a subgrid and resolved contribution, with the latter defined as

$$\text{TKE}_{\text{res}} = \frac{1}{2} \left(\overline{u'u'_{\text{res}}} + \overline{v'v'_{\text{res}}} + \overline{w'w'_{\text{res}}} \right). \quad (25)$$

With the isotropic diffusion approach the subgrid TKE tends to increase for coarsening horizontal grid spacings, and these gradual changes are accompanied by an opposing decrease of the resolved vertical velocity variance. By contrast, with the anisotropic diffusion approach both $\overline{w'w'_{\text{res}}}$ and e tend to diminish simultaneously. This result is likely due to the strong stable thermal stratification that emerges if the horizontal resolution is coarsened. For example, the vertical mean virtual potential temperature profiles presented in Figure 1 indicate that the boundary layer tends to become more stably stratified most notably for coarse horizontal grid spacings $\Delta x_{\text{hor}} \geq 200$ m. A positive vertical gradient of θ_v acts to diminish the stability dependent subgrid factor Equation 19. In addition, following the downgradient diffusion approach it will produce negative subgrid buoyancy fluxes. These two effects both act to diminish the subgrid TKE.

Figure 4 shows the eddy viscosities K_m for the isotropic and anisotropic diffusion approaches. These results were diagnosed with aid of Equation 5 and the subgrid TKE results. For coarsening Δx_{hor} we find that the isotropic eddy viscosity increases. By contrast, the vertical eddy viscosities that are applied in the anisotropic diffusion

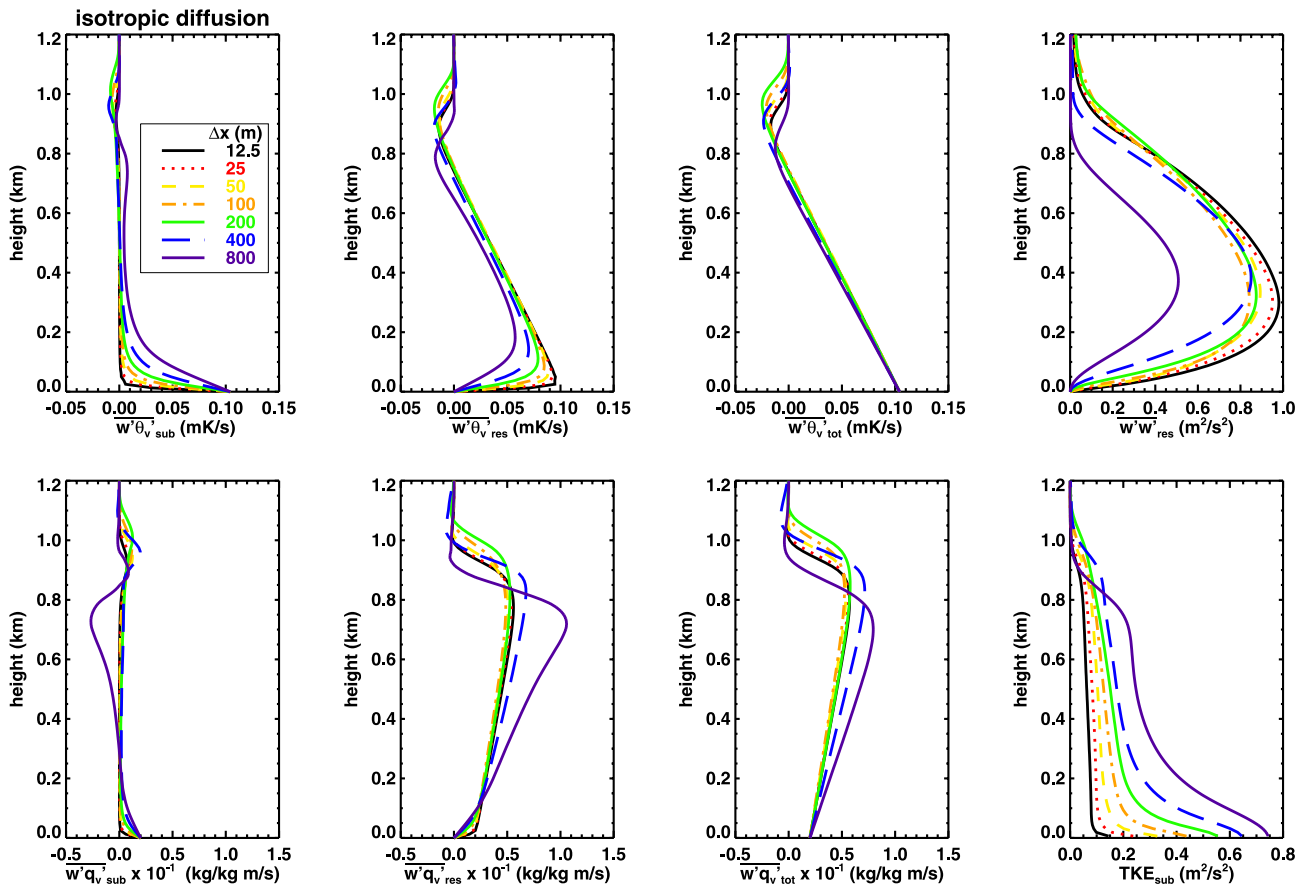


Figure 2. Vertical profiles of the vertical subgrid, resolved and total turbulent fluxes of the virtual potential temperature $\overline{w'\theta'_v}$ and water vapor specific humidity $\overline{w'q'_v}$, respectively, and the resolved vertical velocity variance and subgrid turbulent kinetic energy during the 8th hr of the simulation. The results were obtained with the isotropic diffusion approach. The horizontal grid spacings are according to the legend.

approach, are found to diminish with coarsening Δx_{hor} . Because in all simulations the vertical grid spacing Δz was fixed to a constant value, according to Equations 20 and 21 the respective variations in the vertical eddy viscosity values must be due entirely to the reduction in the subgrid TKE values as shown in Figure 3.

As opposed to the reduced values for the vertical eddy diffusivities, the horizontal eddy viscosities strongly increase with coarsening Δx_{hor} . If the eddy diffusivity becomes excessively large, it will act to dissipate resolved fluctuations too strongly. If, in turn, the vertical turbulent transport becomes dominated by subgrid contributions, as is the case in the surface layer for the simulations with anisotropic diffusion, then reduced values for the vertical eddy diffusivity must be accompanied by enhanced mean vertical gradients in order to support the vertical turbulent fluxes whose near surface values are typically very close to their actual surface values (De Roode, 2007). The erroneous formation of a stable stratification at rather low heights in the boundary layer, such as we observe for coarsening Δx_{hor} and anisotropic diffusion, causes negative subgrid buoyancy fluxes that oppose production of subgrid TKE. Despite the large values for the horizontal eddy diffusivities in this regime, which tend to strongly dissipate resolved fluctuations, the vertical turbulent transports are almost fully dominated by resolved transport. We will show that the scales of this resolved vertical transport are shifted toward larger length scales as compared to the high resolution simulation results.

The strength of the eddy diffusivity determines the dissipation of spectral energy at the smallest length scales. Because the eddy diffusivity is proportional to the square root of the subgrid TKE, and since for coarse horizontal grid spacings the latter depends strongly on the kind of diffusion approach, we will assess whether this impacts the distribution of spectral energies. Furthermore, we will analyze the organization of turbulence structures for the isotropic and anisotropic eddy diffusion approaches by a visual inspection of the instantaneous horizontal fields for some key variables.

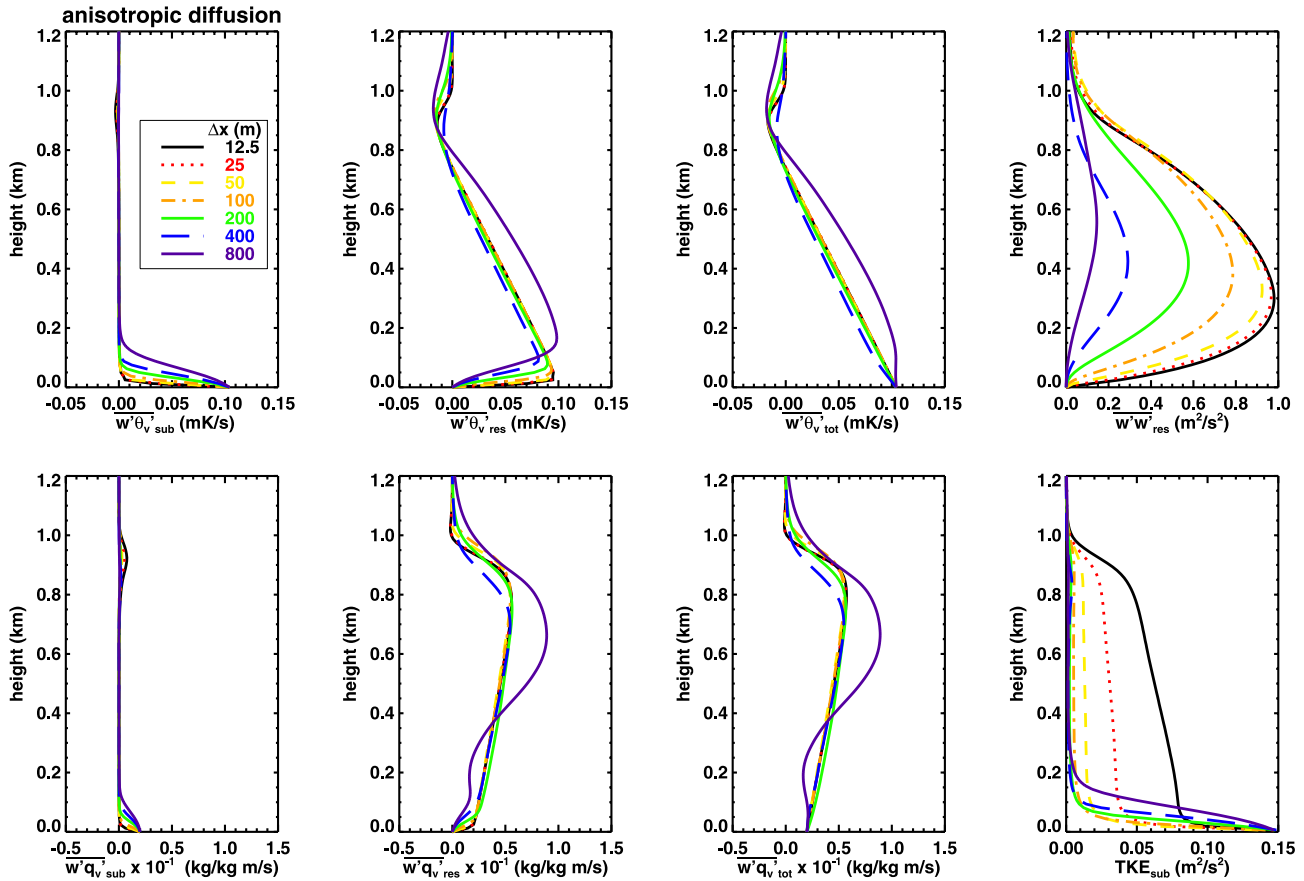


Figure 3. Similar to Figure 2, but in the case the results were obtained with use of the anisotropic diffusion approach. Note that except for the subgrid turbulent kinetic energy the x -axis ranges are the same as in Figure 2.

4.2. Spatial Organization

Figure 5 presents the energy spectra of the three wind velocity components, the potential temperature and the water vapor specific humidity as a function of the wavenumber κ . The spectra were calculated from a Fourier transformation according to De Roode et al. (2004). A comparison of the results with the Reference run shows

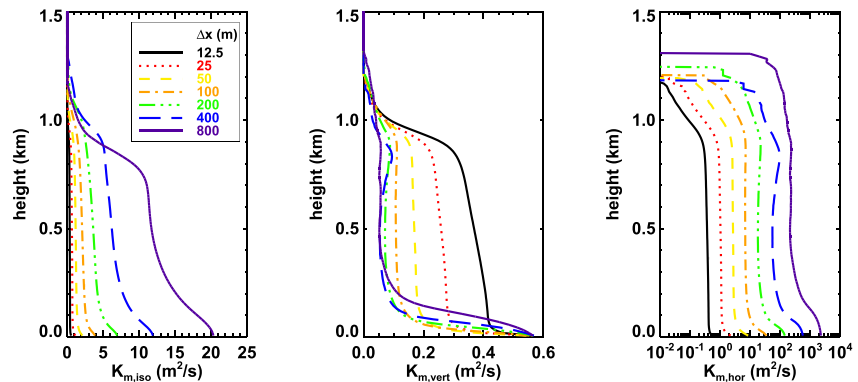


Figure 4. Vertical profiles of the eddy viscosity for the isotropic diffusion approach ($K_{m,iso}$, left panel), and the vertical ($K_{m,vert}$, middle panel) and horizontal ($K_{m,hor}$, right panel) ones for the anisotropic diffusion approach, respectively. The results represent hourly mean horizontal slab-average values as obtained during the last hour of the simulations. Note that to capture the large differences in the horizontal eddy viscosities they are plotted using a logarithmic x -axis. The linestyles and colors are according to the legend.

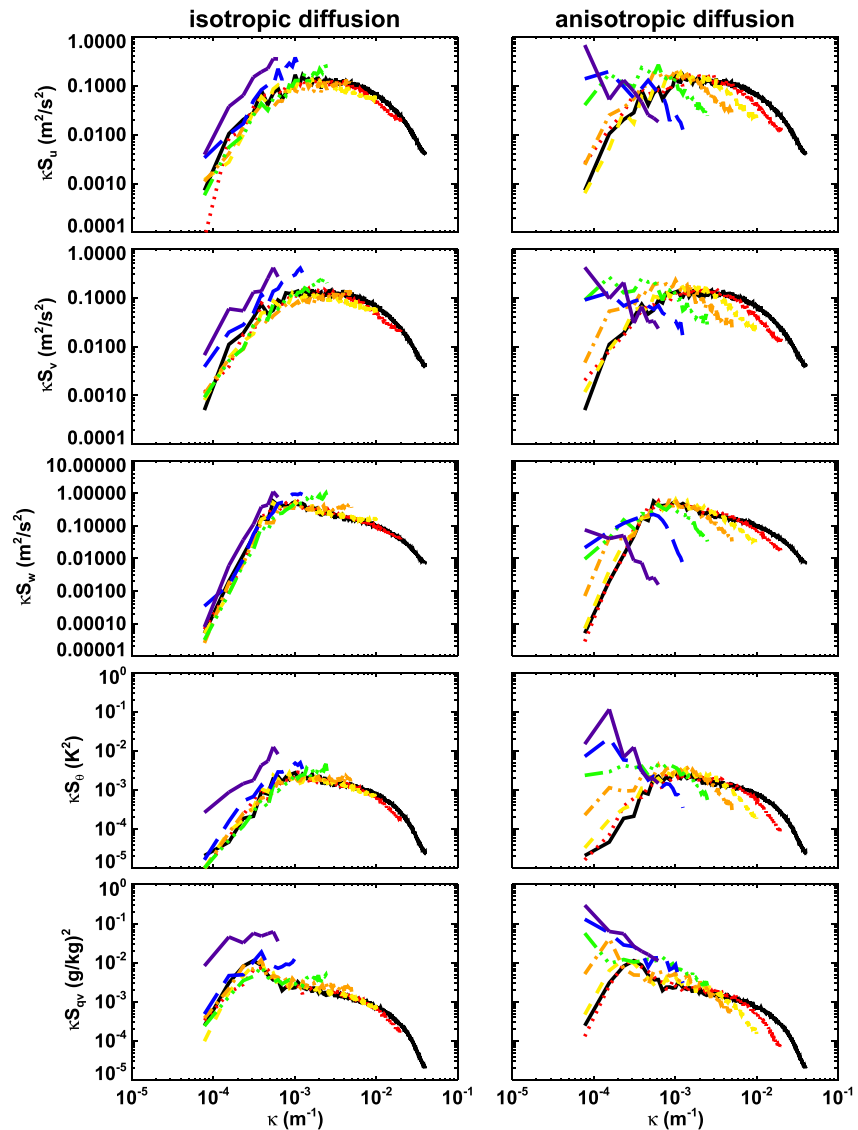


Figure 5. Spectral energy distribution for the horizontal wind components u , v , the vertical wind w , the water vapor specific humidity q_v , and the potential temperature θ , at a height of 356.25 m after 8 hr simulation time. The linestyles and colors are the same as in Figure 3.

that for the anisotropic diffusivity approach a coarsening of Δx_{hor} results in a significant decrease of spectral energies at the largest wavenumbers. This suggests that the increase in the horizontal diffusivity with increasing Δx_{hor} results in a somewhat stronger dissipation at the largest wavenumbers. Interestingly, the decrease of the spectral energies at the largest wavenumbers is partially compensated by an opposite increase at the smallest wavenumbers. In other words, a coarsening of the horizontal grid spacing causes a shift of spectral energy from the largest to the smallest wavenumbers. By contrast, for coarsening horizontal grid spacings the isotropic diffusion approach tends to give only relatively small changes in the spectral energies at the largest resolved wavenumbers. The two sets of simulations have in common that at the smallest wavenumbers the spectral energies tend to increase with respect to the Reference run, although this effect is less prominent for the isotropic diffusion approach.

Figure 6 shows snapshots of the LES fields for the isotropic diffusion approach. The turbulent structures in the simulations that applied isotropic diffusion look similar in terms of their sizes and magnitudes of the fluctuations for horizontal grid spacings Δx_{hor} up to 200 m. The fact that the dominant eddy sizes have length scales of the order of the boundary height, which is located near a height of about 750 m, obviously cannot be resolved with a

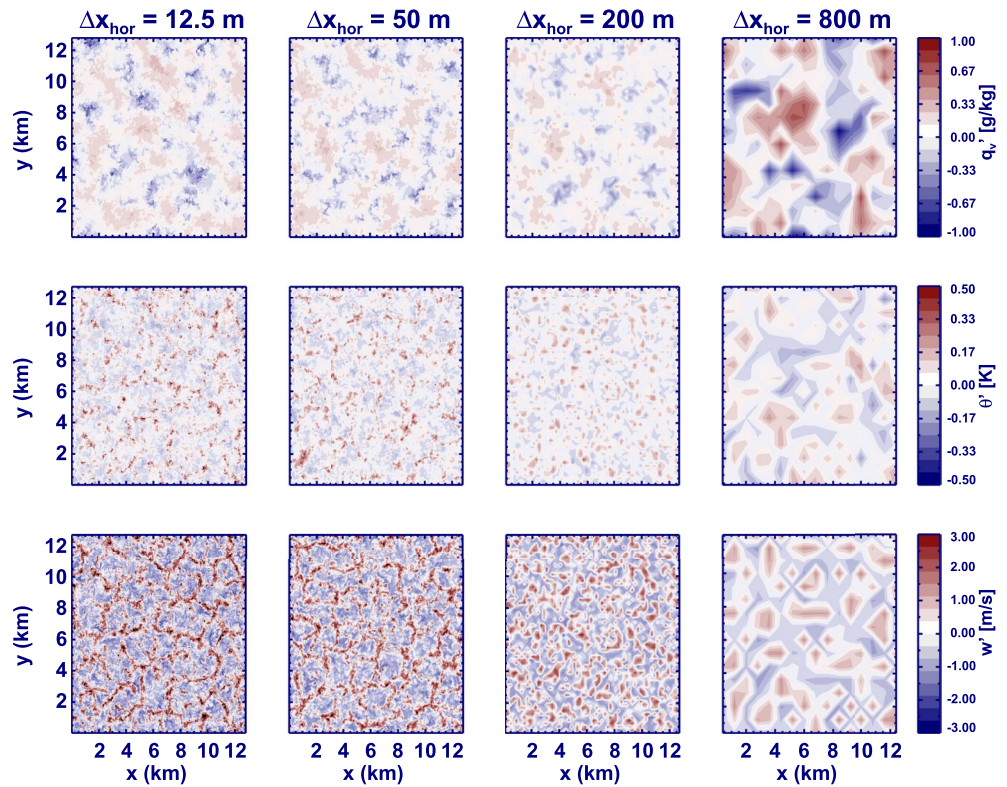


Figure 6. Contour plots of the water vapor specific humidity (upper row), the potential temperature (middle row) and the vertical velocity (lower row) at a height of 356.25 m after 8 hr simulation time as obtained from the simulations applying the isotropic diffusion approach. Each column shows the results for different horizontal grid spacings Δx_{hor} . The range of values shown in the color bars do not reflect the actual minimum and maximum values of the respective variables but are selected to provide an optimum representation of their spatial structures in addition to letting blue, white and red colors representing negative, near zero and positive values, respectively.

horizontal grid spacing of 800 m, and therefore must lead to a coarsening of the spatial structures for all the three variables shown in the figure.

The loss of the spectral energy at the largest wavenumbers, and the shift of the spectral energy toward smaller wavenumbers for coarsening Δx_{hor} for the anisotropic diffusion approach as shown in Figure 5 is clearly visible from the snapshots of the LES fields as shown in Figure 7. Even for a relatively modest grid anisotropy, with $\Delta x_{\text{hor}} = 200$ m, the organization of updrafts changes dramatically to a ring-like structure that is more common to cold pools that develop as a result of evaporation of rain underneath convective clouds. Also the fields of potential temperature and specific humidity become dominated by much larger structures as compared to what is found for smaller values of Δx_{hor} . These results corroborate the results of similar LES runs with anisotropic diffusion and a large value $\Delta x_{\text{hor}} = 1.2$ km presented by Simon and Chow (2021) (see their Figures 4f and 4g).

We will now argue that a change in the horizontal resolution will likely have an impact on the spatial distribution of fluctuations. To this end let us consider the relation between the resolved horizontal slab mean co-variance $\overline{w'\phi'_{\text{res}}}$ of the quantities w and ϕ (their vertical flux), and their co-spectral energy density ($S_{w,\phi}$) (De Roode et al., 2004),

$$\overline{w'\phi'_{\text{res}}} = \int_{\kappa_{\min}}^{\kappa_{\text{Ny}}} S_{w,\phi}(\kappa) d\kappa, \quad (26)$$

with the smallest wavenumber equal to the reciprocal of the horizontal domain size $\kappa_{\min} = 1/L_{\text{hor}}$ and the Nyquist wavenumber is inversely proportional to the horizontal grid spacing $\kappa_{\text{Ny}} = 1/2\Delta x$.

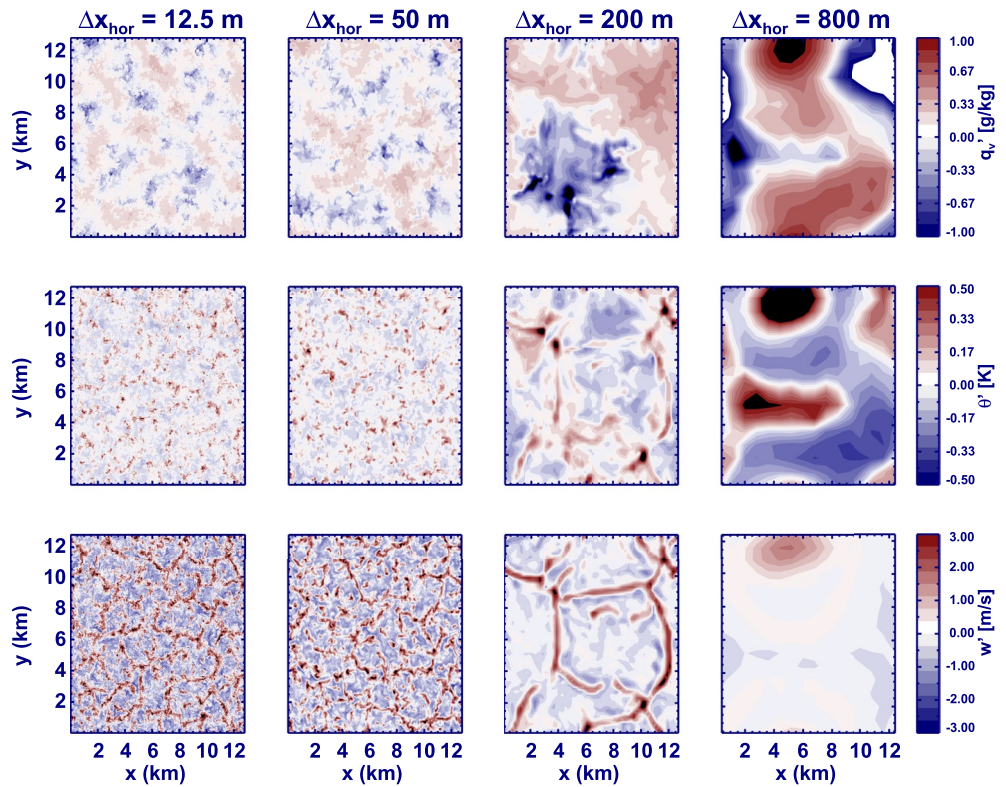


Figure 7. As in Figure 6, but for the anisotropic diffusion approach.

Let us now consider a suite of simulations in which the resolved co-variance is hardly affected by a change in the horizontal resolution. This is the case for the interior of the boundary layers in the majority of the performed runs, as is for example, indicated by the vertical resolved flux profiles for, most notably, q_v in Figures 2 and 3. If variations in the resolved flux contributions are negligibly small, or phrased differently, if $\overline{w'\phi'}_{\text{res}}$ is invariant for changes in Δx , this must consequently result in a change in the shape of the co-spectrum $S_{w,\phi}$. The latter follows from the fact that for a coarsening horizontal grid size the integral over the co-spectrum must remain the same under the constraint of reduced spectral wavenumber interval. Indeed, a change in Δx will result in a change of the largest wavenumber κ_{Ny} according to Equation 26. Likewise the eddy dissipation at the largest wavenumbers can modify the co-spectra in a similar way. If a coarsening grid spacing is accompanied by a stronger dissipation of co-spectral energy at the largest wavenumbers, as is the case for the anisotropic diffusion approach, then conservation of co-variance requires an even stronger shift of fluctuations toward smaller wavenumbers. The vertical profiles of the total slab-mean vertical fluxes are controlled by their surface and top values. In our simulations the same surface flux values ($\overline{w'\phi'}_{\text{sfc}}$) were prescribed, but at the top of the boundary layer the fluxes ($\overline{w'\phi'}_{\text{top}}$) are controlled by the entrainment velocity (w_e) according to the flux-jump relation (Lilly, 1968),

$$\overline{w'\phi'}_{\text{top}} \approx -w_e \Delta\phi, \quad (27)$$

with $\Delta\phi$ the difference of the slab mean value of ϕ across the thermal inversion layer. In a quasi-steady state the (total) vertical flux profiles will have achieved an approximate linear profile,

$$\overline{w'\phi'}(z) = \overline{w'\phi'}_{\text{sfc}} \left(1 - \frac{z}{h}\right) + \overline{w'\phi'}_{\text{top}} \frac{z}{h}. \quad (28)$$

If the entrainment velocity is relatively insensitive to the grid configuration then this will generally result in similar vertical total flux profiles.

We recall that this insensitivity of resolved fluxes to horizontal grid size actually demonstrates an inadequacy of the subgrid TKE model for application on strongly anisotropic grids. But we believe that these results are relevant in the context of research on parameterizations for use in the Gray Zone by numerical weather prediction models.

5. Conclusions

We have presented LES results of a clear convective boundary for a wide range of horizontal grid spacings. Two sets of experiments with different subgrid diffusion approaches were performed. The isotropic diffusion approach applies a single local value for the eddy diffusivity in all three directions. For the Deardorff (1980) subgrid TKE model, and with use of the mesh dependent length scale $\ell = (\Delta x \Delta y \Delta z)^{1/3}$, the isotropic eddy diffusivity can be expressed in terms of a grid anisotropy factor $r = \Delta x_{\text{hor}} / \Delta z$,

$$K_{\text{m,h}} \propto r^{4/3} \Delta z^2. \quad (29)$$

A similar analysis was performed for the anisotropic eddy diffusion approach, a kind of subgrid model that is, as an example, implemented in the SAM LES model. For $r > 1$ the vertical anisotropic diffusivity is smaller than the isotropic value of K_ϕ , but the horizontal diffusivity is larger,

$$\begin{aligned} K_{\text{m,h,vert}} &\propto \Delta z^2, \\ K_{\text{m,h,hor}} &\propto r^2 \Delta z^2 = \Delta x^2. \end{aligned} \quad (30)$$

Note that Deardorff (1980) suggested to use a length scale $\ell = \Delta x_{\text{hor}}$ for a locally unstable atmosphere in terms of its thermal stratification, and a reduced value that accounts for a stable thermal stratification. The use of Δx_{hor} as a length scale for the isotropic eddy diffusion approach will yield $K_\phi \propto \Delta x^2$, similar to the value of the horizontal anisotropic diffusivity.

It is found that a coarsening of the horizontal grid spacing, while keeping the vertical resolution the same, causes the simulation results to diverge from the high resolution reference run that was performed with an isotropic grid. For example, for the isotropic diffusion approach a coarsening of the horizontal grid spacing up to $r = 8$, a grid anisotropy range that is commonly used in LES atmospheric boundary-layer studies, tends to slightly enhance the entrainment velocity at the top of the boundary layer. This finding is likely attributable to the fact that the isotropic eddy diffusivity will increase for increasing horizontal grid spacing according to Equation 29. As more entrainment causes larger heating and drying rates of the boundary layer, and since this can potentially impact a process like the onset of cloud formation, such a sensitivity of modeling results to grid configuration is undesirable. For a grid anisotropy factor in the range $r \leq 8$ this problem is less prominent for the anisotropic diffusion approach, but this somewhat better performance comes with a penalty. Most notably a coarsening of the horizontal grid spacing leads to a stronger dissipation of spectral energies at the largest wavenumbers. It is found that this leads to a shift in the spectral energies toward smaller wavenumbers, as evident from a stronger development of mesoscale fluctuations.

The LES results presented in this study are also relevant in the context of the Gray Zone, in which non-hydrostatic NWP are run at a horizontal resolution that is sufficiently high to start resolving a fraction of the resolved vertical turbulent transport. For highly anisotropic grids, that is, $r > 8$, simulations performed with the isotropic diffusion approach show a better capacity to maintain a vertically well-mixed boundary layer. By contrast, the anisotropic diffusivity formulation as applied in the present study produces a strongly distorted vertical boundary-layer structure, in addition to a striking misrepresentation of the convective scales that tend to increase with coarsening Δx_{hor} . These findings suggest that the usability of this anisotropic diffusion approach seems severely limited.

As a potential remedy to the problems found for the anisotropic diffusion approach at Gray Zone resolutions its formulation might be modified. According to Simon and Chow (2021) such a step could perhaps be taken by applying an enhanced value for the vertical eddy diffusivity for a coarsening horizontal grid. Their parameterization is inspired by a diagnosis of the scale-dependent horizontal and vertical eddy diffusivities from three-dimensional LES fields by Kitamura (2015). In stark contrast with the parameterization for the anisotropic diffusivity applied in the present study, Kitamura (2015) found that the vertical turbulent length scale tends to be larger than the horizontal length scale for coarse horizontal filter lengths. Another hint in this direction is provided by Kurowski and Teixeira (2018) who found that horizontal subgrid fluxes are rather insensitive to the

applied horizontal grid spacing, in contrast to the vertical subgrid fluxes that tend to increase when the horizontal grid is coarsened.

Finally we would like to mention the recent accompanying work by Janssens et al. (2022). They demonstrate an impact of the horizontal grid spacing, among others, on the mesoscale organization of shallow cumulus clouds. This suggests that one should be careful with applying anisotropic grids in large-eddy simulations in particular when it concerns the study on the organization of cloud fields.

Data Availability Statement

The code of the DALES model can be downloaded from <https://github.com/dalessteam/dales> and is also archived on Zenodo (Arabas et al., 2021). The data reported in this study are available from www.euclips.nl/GridAnisotropy/GridAnisotropyPublicData.tar.gz.

Acknowledgments

First of all we wish to thank two anonymous reviewers whose critical reading and constructive remarks helped to improve the manuscript. We would like to thank Joost Dribergen for the implementation of the first version of the anisotropic diffusion approach in DALES and Amber Nusteling for her MSC research project on the scale dependency of the vertical and horizontal eddy diffusivities. We thank Marat Khairoutdinov for fruitful discussions on the anisotropic diffusion approach and Steven van der Linden for critical discussion on the subgrid TKE model. This work is performed as part of the NWO-sponsored national Ruisdael program.

References

- Arabas, S., Axelsen, S., Attema, J., Beets, C., Boeing, S. J., de Bruine, M., et al. (2021). dalesteam/dales: Dales 4.3. Zenodo. <https://doi.org/10.5281/zenodo.4604726>
- Beare, R. J., Macvean, M. K., Holtlag, A. A. M., Cuxart, J., Esau, I., Golaz, J.-C., et al. (2006). An intercomparison of large-eddy simulations of the stable boundary layer. *Boundary-Layer Meteorology*, 118(2), 247–272. <https://doi.org/10.1007/s10546-004-2820-6>
- Boutle, I., Eyre, J., & Lock, A. (2014). Seamless stratocumulus simulation across the turbulent gray zone. *Monthly Weather Review*, 142(4), 1655–1668. <https://doi.org/10.1175/mwr-d-13-00229.1>
- Cuijpers, J., & Duynkerke, P. (1993). Large eddy simulation of trade wind cumulus clouds. *Journal of the Atmospheric Sciences*, 50(23), 3894–3908. [https://doi.org/10.1175/1520-0469\(1993\)050<3894:lesotw>2.0.co;2](https://doi.org/10.1175/1520-0469(1993)050<3894:lesotw>2.0.co;2)
- Deardorff, J. W. (1980). Stratocumulus-capped mixed layers derived from a three-dimensional model. *Boundary-Layer Meteorology*, 18(4), 495–527. <https://doi.org/10.1007/bf00119502>
- De Roode, S. R. (2007). The role of eddy diffusivity profiles on stratocumulus liquid water path biases. *Monthly Weather Review*, 135(7), 2786–2793. <https://doi.org/10.1175/mwr3426.1>
- De Roode, S. R., Duynkerke, P. G., & Jonker, H. J. J. (2004). Large eddy simulation: How large is large enough? *Journal of the Atmospheric Sciences*, 61(4), 403–421. [https://doi.org/10.1175/1520-0469\(2004\)061<0403:ishlil>2.0.co;2](https://doi.org/10.1175/1520-0469(2004)061<0403:ishlil>2.0.co;2)
- De Roode, S. R., Jonker, H. J., van de Wiel, B. J., Vertregt, V., & Perrin, V. (2017). A diagnosis of excessive mixing in Smagorinsky subfilter-scale turbulent kinetic energy models. *Journal of the Atmospheric Sciences*, 74(5), 1495–1511. <https://doi.org/10.1175/JAS-D-16-0212.1>
- Doubrawa, P., & Muñoz-Esparza, D. (2020). Simulating real atmospheric boundary layers at gray-zone resolutions: How do currently available turbulence parameterizations perform? *Atmosphere*, 11(4), 345. <https://doi.org/10.3390/atmos11040345>
- Draxl, C., Allaerts, D., Quon, E., & Churchfield, M. (2021). Coupling mesoscale budget components to large-eddy simulations for wind-energy applications. *Boundary-Layer Meteorology*, 179(1), 73–98. <https://doi.org/10.1007/s10546-020-00584-z>
- Efstathiou, G., Beare, R., Osborne, S., & Lock, A. (2016). Grey zone simulations of the morning convective boundary layer development. *Journal of Geophysical Research: Atmospheres*, 121(9), 4769–4782. <https://doi.org/10.1002/2016jd024860>
- Grylls, T., Suter, I., & van Reeuwijk, M. (2020). Steady-state large-eddy simulations of convective and stable urban boundary layers. *Boundary-Layer Meteorology*, 175(3), 309–341. <https://doi.org/10.1007/s10546-020-00508-x>
- Heinze, R., Dipankar, A., Henken, C. C., Moseley, C., Sourdeval, O., Trömel, S., et al. (2017). Large-eddy simulations over Germany using icon: A comprehensive evaluation. *Quarterly Journal of the Royal Meteorological Society*, 143(702), 69–100. <https://doi.org/10.1002/qj.2947>
- Hellsten, A., Ketelsen, K., Sühring, M., Auvinen, M., Maronga, B., Knigge, C., et al. (2020). A nested multi-scale system implemented in the large-eddy simulation model PALM model system 6.0. *Geosci. Model Development Discussions*, 14(6), 3185–3214.
- Heus, T., van Heerwaarden, C. C., Jonker, H. J. J., Siebesma, A. P., Axelsen, S., van den Dries, K., et al. (2010). Formulation of the Dutch atmospheric large-eddy simulation (DALES) and overview of its applications. *Geoscientific Model Development*, 3(2), 415–444. <https://doi.org/10.5194/gmd-3-415-2010>
- Honnert, R., Efstathiou, G. A., Beare, R. J., Ito, J., Lock, A., Neggers, R., et al. (2020). The atmospheric boundary layer and the “gray zone” of turbulence: A critical review. *Journal of Geophysical Research: Atmospheres*, 125(13), e2019JD030317. <https://doi.org/10.1029/2019jd030317>
- Janssens, M., de Arellano, J. V.-G., van Heerwaarden, C. C., van Stratum, B. J. H., de Roode, S. R., Siebesma, A. P., & Glassmeier, F. (2022). *Shallow convective self-aggregation in large-eddy simulations is sensitive to numerics*. Submitted to JAMES. <https://www.essoar.org/doi/abs/10.1002/essoar.10511889.1>
- Khairoutdinov, M. K., & Randall, D. A. (2005). Cloud-resolving modeling of the ARM summer 1997 IOP: Model formulation, results, uncertainties and sensitivities. *Journal of the Atmospheric Sciences*, 60(4), 607–625. [https://doi.org/10.1175/1520-0469\(2003\)060<0607:crmota>2.0.co;2](https://doi.org/10.1175/1520-0469(2003)060<0607:crmota>2.0.co;2)
- Kitamura, Y. (2015). Estimating dependence of the turbulent length scales on model resolution based on a priori analysis. *Journal of the Atmospheric Sciences*, 72(2), 750–762. <https://doi.org/10.1175/jas-d-14-0189.1>
- Kuroski, M. J., & Teixeira, J. (2018). A scale-adaptive turbulent kinetic energy closure for the dry convective boundary layer. *Journal of the Atmospheric Sciences*, 75(2), 675–690. <https://doi.org/10.1175/jas-d-16-0296.1>
- Leonard, A. (1974). Energy cascade in large-eddy simulations of turbulent fluid flows. In *Advances in geophysics* (Vol. 18, pp. 237–248). Elsevier.
- Lilly, D. (1968). Models of cloud-topped mixed layers under a strong inversion. *Quarterly Journal of the Royal Meteorological Society*, 94(401), 292–309. <https://doi.org/10.1002/qj.49709440106>
- Mason, P. J. (1989). Large-eddy simulation of the convective atmospheric boundary layer. *Journal of the Atmospheric Sciences*, 46(11), 1492–1516. [https://doi.org/10.1175/1520-0469\(1989\)046<1492:lesotc>2.0.co;2](https://doi.org/10.1175/1520-0469(1989)046<1492:lesotc>2.0.co;2)
- Nieuwstadt, F. T., Mason, P. J., Moeng, C.-H., & Schumann, U. (1993). Large-eddy simulation of the convective boundary layer: A comparison of four computer codes. In *Turbulent shear flows* (Vol. 8, pp. 343–367). Springer.

- Ovchinnikov, M., Fast, J. D., Berg, L. K., Gustafson, W. I., Jr., Chen, J., Sakaguchi, K., & Xiao, H. (2022). Effects of horizontal resolution, domain size, boundary conditions, and surface heterogeneity on coarse LES of a convective boundary layer. *Monthly Weather Review*, 150, 1397–1415. <https://doi.org/10.1175/MWR-D-21-0244.1>
- Schalkwijk, J., Jonker, H. J., Siebesma, A. P., & Bosveld, F. C. (2015). A year-long large-eddy simulation of the weather over Cabauw: An overview. *Monthly Weather Review*, 143(3), 828–844. <https://doi.org/10.1175/mwr-d-14-00293.1>
- Simon, J. S., & Chow, F. K. (2021). Alternative anisotropic formulations for eddy-viscosity models in the weather research and forecasting model. *Boundary-Layer Meteorology*, 181(1), 11–37. <https://doi.org/10.1007/s10546-021-00642-0>
- Stevens, B., Moeng, C., Ackerman, A. S., Bretherton, C. S., Chlond, A., de Roode, S. R., et al. (2005). Evaluation of large-eddy simulations via observations of nocturnal marine stratocumulus. *Monthly Weather Review*, 133(6), 1443–1462. <https://doi.org/10.1175/mwr2930.1>
- Stevens, B., Vali, G., Comstock, K., Wood, R., van Zanten, M. C., Austin, P. H., et al. (2005). Pockets of open cells (POCs) and drizzle in marine stratocumulus. *Bulletin America Meteorology Social*, 86(1), 51–57. <https://doi.org/10.1175/bams-86-1-51>
- Sullivan, P. P., Moeng, C.-H., Stevens, B., Lenschow, D. H., & Mayor, S. D. (1998). Structure of the entrainment zone capping the convective atmospheric boundary layer. *Journal of the Atmospheric Sciences*, 55(19), 3042–3064. [https://doi.org/10.1175/1520-0469\(1998\)055<3042:sotezc>2.0.co;2](https://doi.org/10.1175/1520-0469(1998)055<3042:sotezc>2.0.co;2)
- Sullivan, P. P., & Patton, E. G. (2011). The effect of mesh resolution on convective boundary layer statistics and structures generated by large-eddy simulation. *Journal of the Atmospheric Sciences*, 68(10), 2395–2415. <https://doi.org/10.1175/jas-d-10-05010.1>
- van Hoof, J. A., Baas, P., van Tiggelen, M., Anson, C., & van de Wiel, B. J. (2019). An idealized description for the diurnal cycle of the dry atmospheric boundary layer. *Journal of the Atmospheric Sciences*, 76(12), 3717–3736. <https://doi.org/10.1175/jas-d-19-0023.1>
- Van der Dussen, J. J., de Roode, S. R., Ackerman, A. S., Blossey, P. N., Bretherton, C. S., Kurowski, M. J., et al. (2013). The GASS/EUCLIPSE model intercomparison of the stratocumulus transition as observed during ASTEX: LES results. *Journal of Advances in Modeling Earth Systems*, 5(3), 483–499. <https://doi.org/10.1002/jame.20033>
- Van Zanten, M. C. (2000). *Entrainment processes in stratocumulus* (Doctoral dissertation) (p. 139). Utrecht University.
- Van Zanten, M. C., Stevens, B., Nuijens, L., Siebesma, A. P., Ackerman, A., Burnet, F., et al. (2011). Controls on precipitation and cloudiness in simulations of trade-wind cumulus as observed during RICO. *Journal of Advances in Modeling Earth Systems*, 3(2), M04001. <https://doi.org/10.3894/JAMES.2011.3.5>
- Wing, A. A., Stauffer, C. L., Becker, T., Reed, K. A., Ahn, M.-S., Arnold, N. P., et al. (2020). Clouds and convective self-aggregation in a multi-model ensemble of radiative-convective equilibrium simulations. *Journal of Advances in Modeling Earth Systems*, 12(9), e2020MS002138. <https://doi.org/10.1029/2020ms002138>